



OPEN ACCESS

EDITED BY
Paolo Capuano,
University of Salerno, Italy

REVIEWED BY
Jiabing Zhang,
Guangxi University, China
Umberto Tammaro,
Istituto Nazionale di Geofisica e
Vulcanologia (INGV), Italy

*CORRESPONDENCE
Zhonghua Jiang,
✉ jiangzh@stu.cqu.edu.cn

RECEIVED 28 November 2025
REVISED 30 January 2026
ACCEPTED 09 February 2026
PUBLISHED 24 February 2026

CITATION
Zhang R, Li X, Wang Y, Qi Z, He Z, Li M
and Jiang Z (2026) Ground surface
deformation induced by grouting
construction of shallow-buried shield
tunnels in mudstone strata.
Front. Earth Sci. 14:1756354.
doi: 10.3389/feart.2026.1756354

COPYRIGHT
© 2026 Zhang, Li, Wang, Qi, He, Li and
Jiang. This is an open-access article
distributed under the terms of the
[Creative Commons Attribution License
\(CC BY\)](https://creativecommons.org/licenses/by/4.0/). The use, distribution or
reproduction in other forums is
permitted, provided the original
author(s) and the copyright owner(s) are
credited and that the original
publication in this journal is cited, in
accordance with accepted academic
practice. No use, distribution or
reproduction is permitted which does
not comply with these terms.

Ground surface deformation induced by grouting construction of shallow-buried shield tunnels in mudstone strata

Rong Zhang^{1,2,3}, Xiaochuan Li⁴, Yue Wang⁴, Zhengping Qi⁴,
Zhenqiang He⁴, Ming Li⁴ and Zhonghua Jiang^{1,2*}

¹School of Civil Engineering, Chongqing University, Chongqing, China, ²State Key Laboratory of Safety and Resilience of Civil Engineering in Mountain Area, Chongqing, China, ³Chongqing Rail Transit Design and Research Institute Company, Chongqing, China, ⁴Powerchina Sinohydro Engineering Bureau 4 Co., Ltd, Xining, China

Grouting is widely used to mitigate ground surface deformation during shield tunneling. However, the quantitative influence of grout solidification and hardening on deformation and its prediction remains insufficiently understood. This work investigates how time-dependent grout solidification and hardening affect ground deformation. It combines analytical solutions with numerical simulations. The time-dependent evolution of grout properties is incorporated into both approaches for shallow-buried shield tunneling in mudstone strata. Results show that explicitly simulating grout solidification yields larger settlement than neglecting it. Compared with the instantaneous setting case (0 h), an initial setting time of 4 h increases the maximum surface settlement by 59%. The grout hardening rate plays a decisive role in deformation control. Theoretical analyses further indicate that the shield tail, rather than the cutterhead, is the critical reference location governing deformation development.

KEYWORDS

analytical method, metro shield tunneling, mudstone strata, numerical simulation, synchronous grouting

1 Introduction

Shield tunneling has become the predominant construction method in metro tunnel engineering owing to its advantages of minimal environmental impact, high automation, and rapid excavation speed (Goh et al., 2018; Komiya et al., 2001; Song et al., 2023; Liu B. et al., 2021). To ensure smooth advancement of the shield machine, a difference is deliberately maintained between the cutterhead excavation diameter and the external diameter of the segment lining, which inevitably generates a tail gap once the segments are released from the shield tail (Cao et al., 2024; Wang et al., 2019; Zheng et al., 2020). The formation of this tail gap induces contraction of the surrounding soil and rock, constituting a major factor contributing to ground deformation. To mitigate such deformation, synchronous grouting is commonly adopted (Huang et al., 2020; Lou et al., 2022). In urban areas, however, stringent regulations impose strict limits on ground surface deformation during metro tunnel construction (Kong et al., 2022; Wang et al., 2022). This necessitates a clear understanding of the deformation patterns induced by shield tunneling and the controlling mechanism of grouting, thereby enabling both the prediction and effective mitigation of surface deformation (Liu et al., 2023). In practical shallow-buried shield tunneling, inadequate

control of synchronous grouting, delayed grout solidification, and the time-dependent deformation of mudstone frequently lead to excessive ground settlement and segmental dislocation. These engineering problems highlight the need for a clearer understanding of the interaction between grouting behavior and ground response under real construction conditions.

To meet these requirements, many scholars have conducted relevant studies. [Alsirawan et al. \(2023\)](#), [Ağbay and Topal \(2020\)](#), [Goh et al. \(2018\)](#), [Qiao et al. \(2010\)](#), and [Zhang et al. \(2023\)](#) focused on the determination of maximum ground settlement values. However, surface deformation does not occur uniformly within a certain range, and differential settlement is often more detrimental to surface structures. Therefore, obtaining two- and three-dimensional distributions of ground deformation is considered a more rational objective ([Franzius et al., 2004](#); [Ocak, 2014](#); [Shahin et al., 2016](#); [Wang et al., 2009](#)). [Peck \(1969\)](#) first proposed the concept of ground loss and suggested that ground settlement caused by tunnel excavation in soil follows a Gaussian distribution. Similar findings have been reported for shield tunneling-induced settlement by [Mair et al. \(1993\)](#), [Dong et al. \(2022\)](#), and [Fang et al. \(2014\)](#). In addition to settlement, [Cui et al. \(2024\)](#), by integrating numerical simulation with theoretical analysis, demonstrated that shield tunneling can also induce heave deformation in both the strata and the ground surface.

Beyond clarifying the distribution patterns of ground deformation induced by shield tunneling, it is also necessary to investigate the influence of different grouting parameters on deformation control, with the aim of developing optimized grouting schemes ([Ding et al., 2021](#)). [Anato et al. \(2021\)](#) confirmed through numerical simulations that grout material properties are critical factors for settlement control. [Kavvadas et al. \(2017\)](#) and [Liang et al. \(2025\)](#) showed that high-performance grout can effectively control ground deformation and compensate for settlement. Previous studies indicate that parameters such as the initial setting time, ultimate strength, strength growth rate, and grouting pressure significantly affect the efficiency of synchronous grouting in controlling ground deformation ([Mooney et al., 2016](#); [Yang et al., 2023](#)). [Meng et al. \(2018\)](#) and [Zhang et al. \(2023\)](#) further demonstrated that grout materials characterized by short setting times, high elastic modulus, and low shear strength are more effective in controlling ground deformation.

These studies not only highlight the significant influence of grout properties on ground deformation during shield tunneling but also propose various calculation methods for surface settlement. Nonetheless, the mechanisms by which specific grout hardening characteristics influence ground and surface deformation remain unclear. Moreover, the methods currently used to calculate shield tunneling-induced surface deformation require further refinement.

Nevertheless, two issues remain insufficiently addressed in existing studies. First, grout-related parameters (e.g., setting time, stiffness and strength development) are often treated as static inputs or are represented only by a final hardened state, while the early-stage transition from a fluid-like grout to a load-bearing solid is inherently time-dependent and can strongly influence deformation evolution immediately after tail gap formation ([Wang et al., 2025](#)). Second, many longitudinal deformation formulations implicitly take the tunnel face as the reference location for deformation

development ([Abdelaziz et al., 2023](#)). For shield tunneling in weak rock formations such as mudstone, however, the shield shell provides substantial temporary support, and pronounced deformation tends to develop rapidly near the shield tail due to segment release, tail gap formation and synchronous grouting. These features motivate the present work to explicitly consider grout solidification and hardening characteristics and to revisit the appropriate longitudinal reference location for describing settlement development.

With respect to research methodologies, [Tian et al. \(2023\)](#), [Deng et al. \(2021\)](#), [Zhang et al. \(2023\)](#) and [Han et al. \(2025\)](#) calculated ground deformation using numerical simulations, whereas [Kong et al. \(2019\)](#), [Zhou et al. \(2021\)](#), and [Shi et al. \(2017\)](#) employed theoretical analysis to study the deformation induced by shield tunneling. Both approaches yielded reliable results, indicating that combining numerical simulations and theoretical solutions provides a reasonable basis for deformation calculations. To ensure practical applicability of theoretical results, the present study not only employs numerical simulations and analytical solutions but also validates the findings against field data.

Based on the engineering conditions of Chongqing Metro Line 27, this work combines steady-state numerical simulations in COMSOL Multiphysics with two analytical calculation approaches to investigate ground deformation induced by synchronous grouting in shallow-buried shield tunnels in mudstone strata. The main objectives are: (i) to quantify the influence of grout solidification and hardening characteristics (particularly initial setting time) on surface and strata deformation; (ii) to clarify the deformation development mechanism and identify the critical reference location along the tunnel axis; and (iii) to improve the applicability of existing analytical solutions through calibrated correction parameters and field-data validation.

2 Methods

2.1 Theoretical solution of ground surface deformation induced by shield tunneling

A geometric model is established, assuming the tunnel is excavated along the positive y -axis, which $y = 0$ represents the location of the tunnel's face. The x -axis lies on the ground surface and is perpendicular to the tunnel axis, while the z -axis represents the vertical direction, as illustrated in [Figure 1](#).

Neglecting the elliptical deformation of segment lining resulting from long-term service, and based on the cavity contraction theory within soil proposed by [Sen \(1951\)](#), [Mindlin and Cheng \(1950\)](#), as well as the theory of uniform radial contraction proposed by [Sagaseta \(1987\)](#), it is assumed that the volume loss caused by lining contraction during excavation is $V = 2\pi R\mu_\epsilon$. [Pinto and Whittle \(2014\)](#) derived theoretical solutions for the three-dimensional surface deformation field, which are expressed as [Equations 1–3](#):

$$u_{x0} = -\frac{V}{\pi} \cdot \frac{(1-\nu)x}{x^2 + H^2} \cdot \frac{\sqrt{x^2 + y^2 + H^2} - y}{\sqrt{x^2 + y^2 + H^2}} \quad (1)$$

$$u_{y0} = -\frac{V}{\pi} \cdot \frac{(1-\nu)}{\sqrt{x^2 + z^2 + H^2}} \quad (2)$$

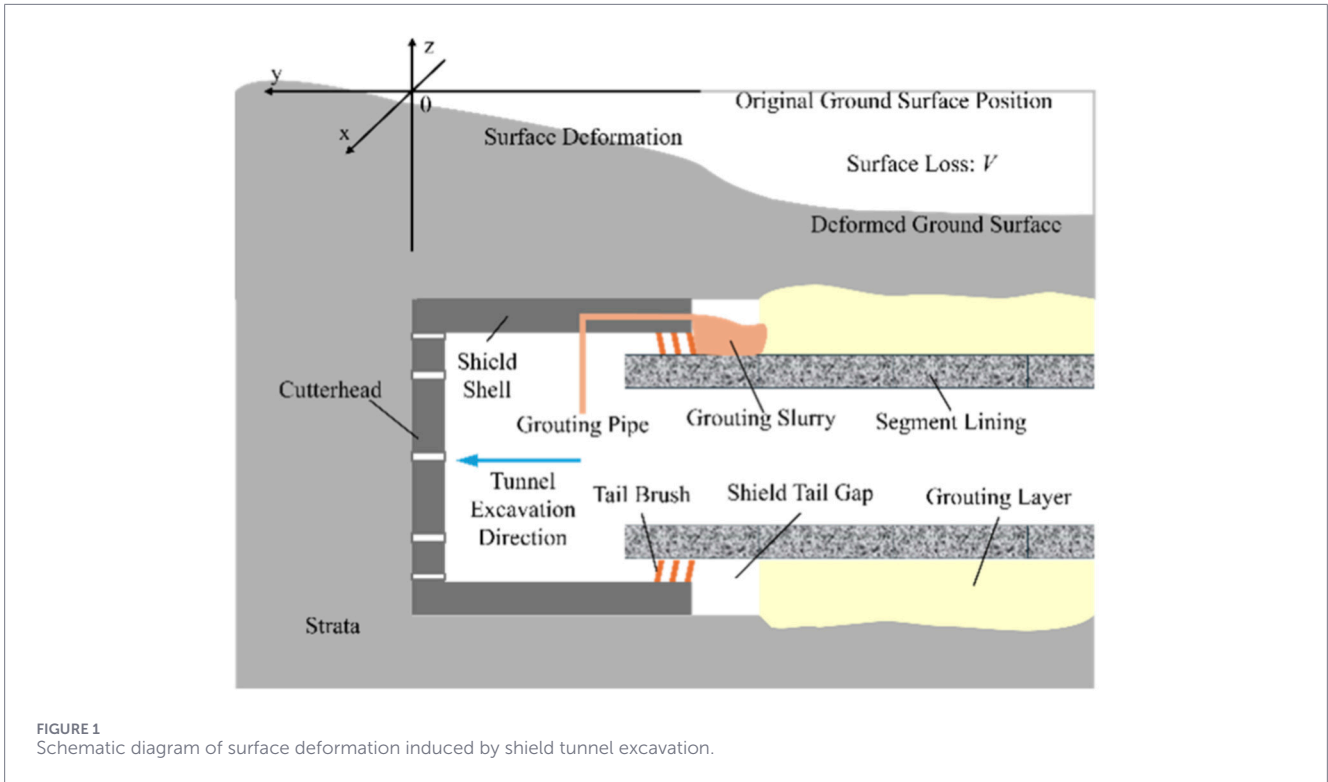


FIGURE 1 Schematic diagram of surface deformation induced by shield tunnel excavation.

$$u_{z0} = -\frac{V}{\pi} \cdot \frac{(1-\nu)H}{x^2 + H^2} \cdot \frac{\sqrt{x^2 + y^2 + H^2} - y}{\sqrt{x^2 + y^2 + H^2}} \quad (3)$$

In these equations, u_{x0} , u_{y0} and u_{z0} represent the displacement components in the x, y, and z directions, respectively; ν denotes the Poisson's ratio of the soil or rock mass; u_ϵ is the radial contraction of the tunnel lining; R and H are the tunnel radius and the depth of the tunnel axis, respectively.

For Equation 3, by neglecting soil compressibility and taking Poisson's ratio of the ground as 0.5, and setting $y = -\infty$ to represent a stabilized settlement condition, the vertical displacement along the x-direction can be simplified as Equation 4:

$$u_{z0} \Big|_{y \rightarrow -\infty}^{v=0.5} = -2u_\epsilon R \frac{H}{x^2 + H^2} \quad (4)$$

In fact, Equation 4 is identical to the two-dimensional analytical solution proposed by Verruijt and Booker (1996) for surface deformation induced by tunnel excavation. However, field monitoring data from actual engineering projects have shown that this model does not provide accurate predictions of surface settlement. Therefore, Yang et al. (2020) introduced an improved formulation for the displacement component u_{z0} by incorporating correction coefficients in three spatial dimensions. As a result, Equation 3 was modified to Equation 5, and Equation 4 was refined into Equation 6:

$$u'_{z0} = -\lambda_1 u_\epsilon R \cdot \frac{H}{(\lambda_2 x)^2 + H^2} \cdot \frac{\sqrt{(\lambda_2 x)^2 + (\lambda_3 y)^2 + H^2} - \lambda_3 y}{\sqrt{(\lambda_2 x)^2 + (\lambda_3 y)^2 + H^2}} \quad (5)$$

$$u'_{z0} \Big|_{y \rightarrow -\infty}^{v=0.5} = -2\lambda_1 u_\epsilon R \frac{H}{(\lambda_2 x)^2 + H^2} \quad (6)$$

In these equations, λ_1 is the correction parameter for the maximum settlement value, λ_2 is the correction parameter for the settlement trough width, and λ_3 is the correction parameter for the settlement trough length.

The correction principle in the x-axis direction is illustrated in Figure 2. Clearly, the value of V remains unchanged before and after the correction. Therefore:

$$\int_{-\infty}^{+\infty} \int_{-\infty}^{+\infty} u'_{z0} dx dy = \int_{-\infty}^{+\infty} \int_{-\infty}^{+\infty} u_{z0} dx dy \quad (7)$$

By solving Equation 7 with respect to the x-axis and the x-y plane, respectively, the results are presented in Equations 8, 9:

$$\lambda_1 = \lambda_2 = \lambda \quad (8)$$

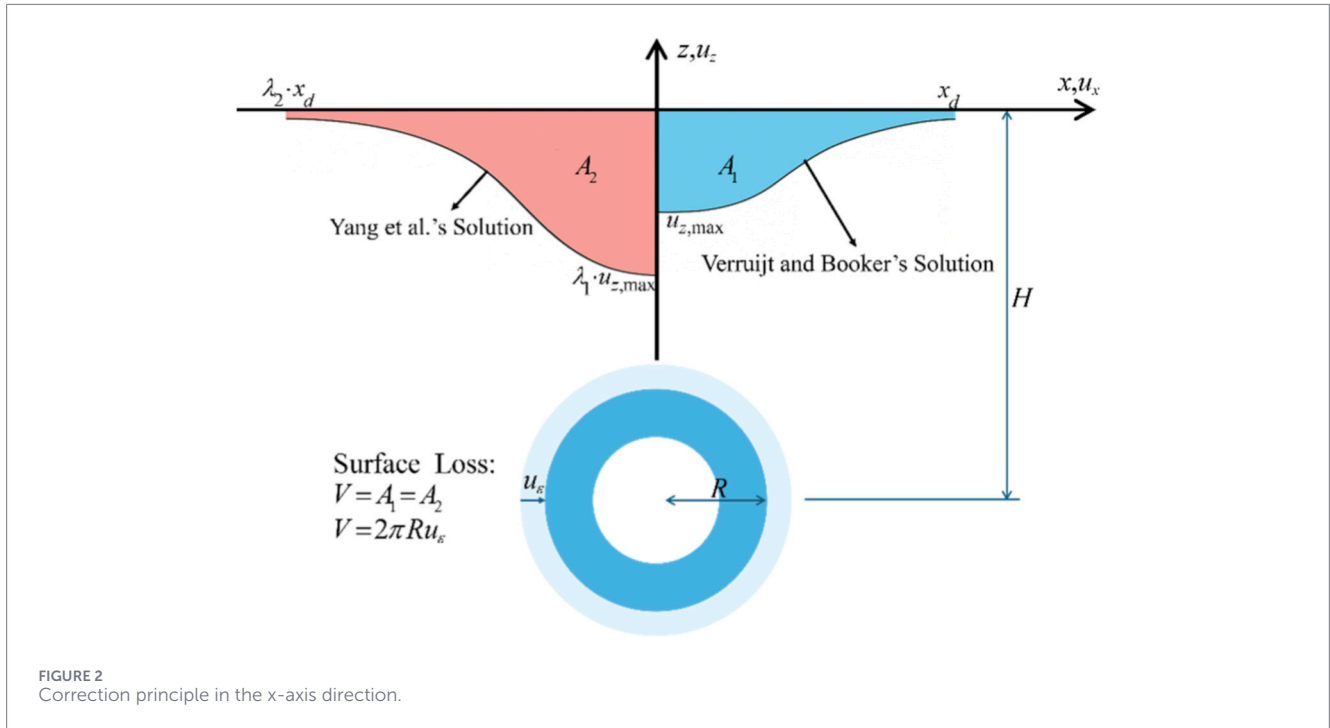
$$\lambda_3 = 1 \quad (9)$$

Thus, the three-dimensional surface deformation induced by tunnel excavation can be corrected and expressed as Equation 10:

$$u'_{z0} = -\lambda u_\epsilon R \cdot \frac{H}{(\lambda x)^2 + H^2} \cdot \frac{\sqrt{(\lambda x)^2 + y^2 + H^2} - y}{\sqrt{(\lambda x)^2 + y^2 + H^2}} \quad (10)$$

Therefore, the vertical deformation in the x-direction can be simplified as Equation 11:

$$u'_{z0} \Big|_{y \rightarrow -\infty}^{v=0.5} = -2\lambda u_\epsilon R^2 \frac{H}{(\lambda x)^2 + H^2} \quad (11)$$



The settlement expression in the y -direction is given by (see Equation 12):

$$u'_{z0} \Big|_{x=0}^{y=0.5} = -\frac{\lambda u_\epsilon R}{H} \cdot \frac{\sqrt{y^2 + H^2} - y}{\sqrt{y^2 + H^2}} \quad (12)$$

In their study, Yang et al. (2020) determined the empirical value of λ through model tests, as shown in Equation 13:

$$\lambda = 0.514 + 3.356e^{-2.466 \frac{R}{H}} \quad (13)$$

The correction principle in the y -direction is illustrated in Figure 3. The correction only amplifies the maximum surface deformation by a factor of λ , without altering the distribution pattern or variation trend of the surface deformation. This implies that the second derivative of the surface settlement distribution curve in the y -direction remains the same before and after the correction. Moreover, in both solutions, the surface settlement directly above the tunnel face corresponds to half of the maximum post-excavation surface settlement.

However, both field monitoring and subsequent numerical simulation studies indicate that in mudstone strata, the assumption of $y=0$ representing the position of the tunnel face may not be appropriate due to the significant support provided by the shield shell. Therefore, in addition to the conventional approach for calculating surface deformation induced by shallow-buried shield tunneling in mudstone, this study also adopts an alternative method in which $y=0$ denotes the location of tail grouting.

This is not a simple translation of the settlement surface along the negative y -axis by a distance equal to the length of the shield shell l ; rather, it requires the introduction of a parameter y' as the coordinate reference along the y -axis. The

difference between the two approaches lies in the value of y' : the former method uses $y' = y$, while the latter uses $y' = y + l$. For the case study project—Chongqing Metro Line 27—the shield shell length measured on-site is $l = 10.8m$, as shown in Figure 3 and Equation 14.

$$u'_{z0} = -\lambda u_\epsilon R \cdot \frac{H}{(\lambda x)^2 + H^2} \cdot \frac{\sqrt{(\lambda x)^2 + y'^2 + H^2} - y'}{\sqrt{(\lambda x)^2 + y'^2 + H^2}} = \begin{cases} -\lambda u_\epsilon R \cdot \frac{H}{(\lambda x)^2 + H^2} \cdot \frac{\sqrt{(\lambda x)^2 + y^2 + H^2} - y}{\sqrt{(\lambda x)^2 + y^2 + H^2}} \\ \text{or} \\ -\lambda u_\epsilon R \cdot \frac{H}{(\lambda x)^2 + H^2} \cdot \frac{\sqrt{(\lambda x)^2 + (y+l)^2 + H^2} - (y+l)}{\sqrt{(\lambda x)^2 + (y+l)^2 + H^2}} \end{cases} \quad (14)$$

2.2 Modeling and analysis

The shield machine concurrently performs both tunnel face excavation and support of the surrounding ground. As the segment lining is assembled, the gap at the shield tail is immediately filled with grout. The grout gradually hardens, and the grouting pressure slowly dissipates, thereby providing support to the surrounding strata. The factors involved in this process are illustrated in Figure 4.

2.2.1 Simulation of construction stages

To achieve a simplified yet effective simulation of shield tunnel construction, the first step is to set the step parameters, which replace the time variable and define all field variables and function

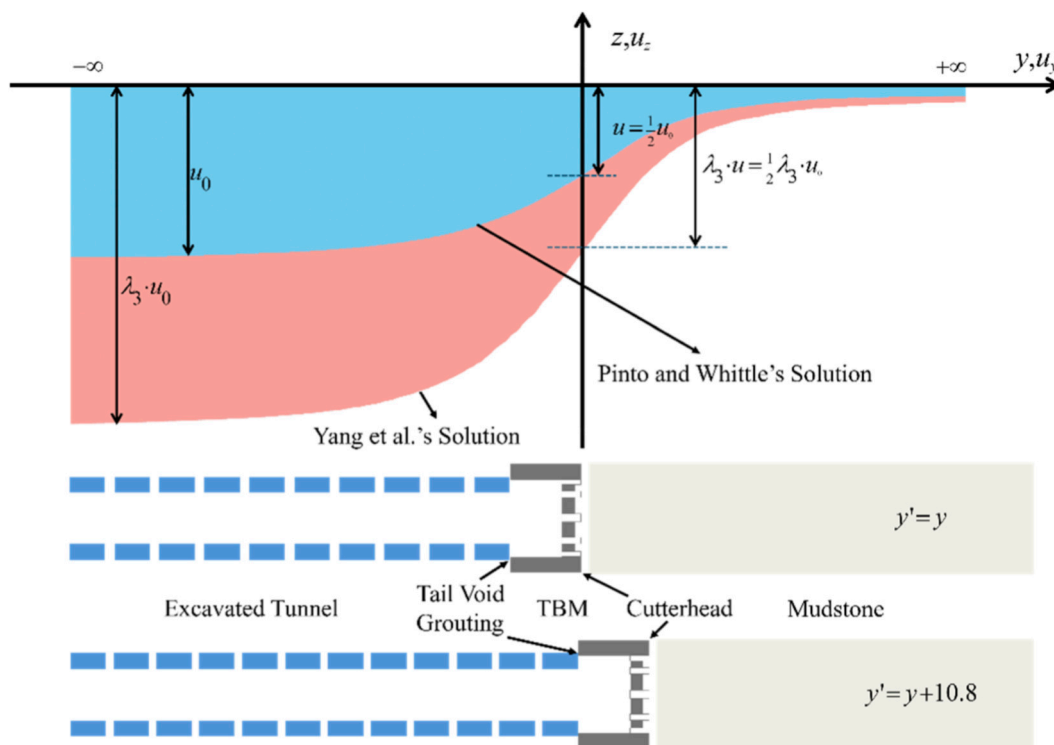


FIGURE 3 Correction principle in the y-axis direction and the two calculation methods.

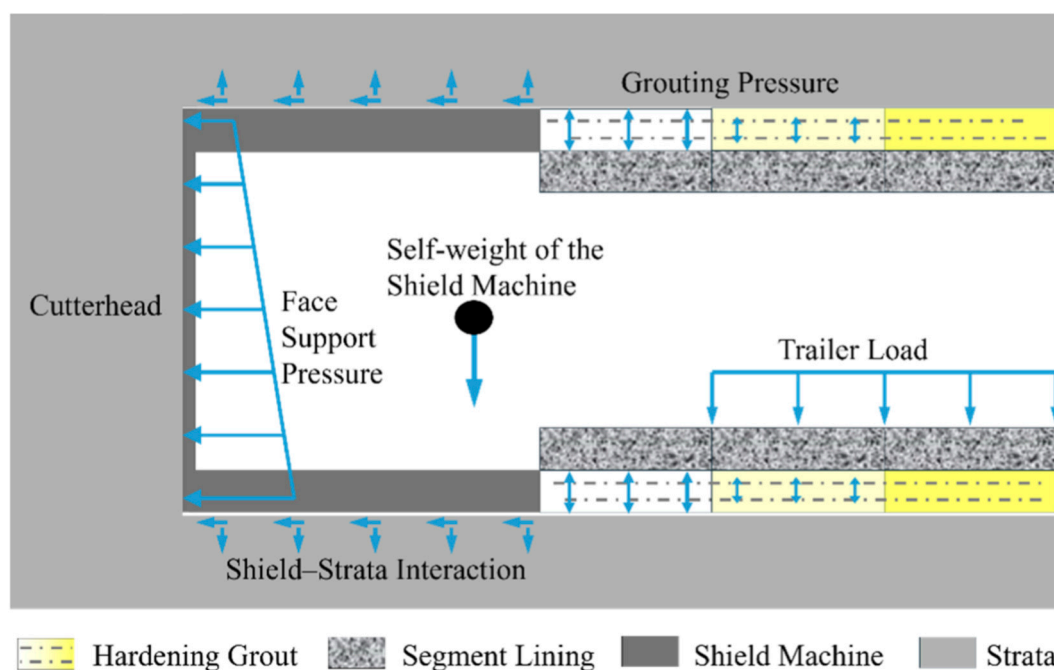


FIGURE 4 Simulated factors in shield tunnel construction.

commands within the model. The model uses solid mechanics to solve the physical field and is set to a steady-state analysis, as it focuses on capturing the final deformation state after construction steps, reducing computational cost while providing an accurate representation of long-term deformation. This approach simplifies the process and ensures efficient simulation, especially for large-scale tunneling projects.

The solution of the model requires the initial stress state to be based on the results from the previous step. Typically, the auxiliary scanning function is used to import the calculation results from the previous step as external stress. During the construction process, excavation of the geotechnical body, activation of the segment lining and grouting layer, and the advancement of the shield machine are involved. The activation and deactivation of these elements must be carried out using the “activation” function. Specifically, an activation expression and activation factor need to be defined. Using the centroid coordinate operator “centroid” in conjunction with the step parameters, a judgment expression is written. When the activation expression is satisfied, it is evaluated as 1, and the domain is activated accordingly.

2.2.2 Element and interaction modeling

In the modeling process, the shield shell is constructed using solid elements. Its self-weight is simulated by assigning an increased equivalent density to represent the shield machine mass realistically (Alsahly et al., 2016; Liu C. et al., 2021). The segment lining is modeled as a homogenized circular ring with reduced stiffness, using a reduction factor of 0.3 to reflect the mechanical behavior of assembled segments (Liu C. et al., 2021). For the surrounding soil and rock mass, the Drucker–Prager model is adopted to describe the elastoplastic behavior. When configuring the plasticity model in COMSOL Multiphysics, selecting the “Match Mohr–Coulomb model” option allows direct input of equivalent parameters for the Drucker–Prager model. It should be noted that although mudstone exhibits creep behavior, the deformation associated with synchronous grouting and the initial setting of grout occurs within a short construction timescale, during which the creep effect of mudstone is negligible. Therefore, creep is not included in the theoretical formulation without affecting the applicability of the analytical results.

The contact between the shield machine and the surrounding geotechnical body, the segment lining and the grouting layer, as well as the strata, is modeled using Coulomb friction for the tangential behavior and penalty functions for the normal behavior. This contact is represented by establishing a contact relationship between the outer surface of the shield and the inner surface of the tunnel’s circumferential excavation face.

In the solid mechanics physics field of COMSOL Multiphysics, an assembly is first created during the geometry model setup. Then, a contact pair is manually or automatically defined, and the contact behavior between the pairs is specified to simulate real-world contact interactions. After the segment lining is installed and the synchronous grouting process is completed, a towing load needs to be applied. Specifically, a line load of magnitude 50,000 N/m is applied to the segment lining.

2.2.3 Simulation of grout hardening

The grouting layer, located between the segment lining and the surrounding ground, is typically simplified as a homogeneous elastic circular ring in numerical models. Material randomness and heterogeneity are neglected to streamline the analysis. The thickness of the grouting layer is set to the theoretical value of the shield tail gap, representing the designed annular space between the lining and the excavation boundary.

The grouting material is injected in a fluid state into the gap behind the shield tail, gradually undergoing a hardening phase change over time. This process is accompanied by the dissipation of grouting pressure and the increase in the material’s mechanical properties. Although this process is inherently time-dependent, the steady-state analysis used in this study simplifies the grout hardening to a final, stabilized state, which reduces computational demands and focuses on capturing the long-term deformation effects. The influence of grout hardening over time is therefore represented in terms of its final mechanical properties at the end of the grouting process. This process can be represented through a fitting function (Kasper and Meschke, 2006; Lambrugh et al., 2012). Initially, the grout behaves as a non-elastic, non-Newtonian fluid; upon final setting, it transforms into a solid with stable mechanical characteristics. To simulate this fluid-to-solid transformation using only the Solid Mechanics physics module, the following assumptions are made: before initial setting, the grout has an elastic modulus of 0 MPa and a Poisson’s ratio of 0.5, representing an incompressible fluid-like state, and these pre-setting parameters are based on the assumed behavior of a non-elastic, non-Newtonian fluid. After final setting, the elastic modulus increases to 800 MPa and Poisson’s ratio decreases to 0.3, representing a solid state, with these post-setting mechanical properties determined from laboratory tests of the grout used at the project site. To investigate the influence of setting time on ground deformation, four comparative cases are defined based on different initial setting times: 0 h, 1 h, 2 h, and 4 h. The final setting time is uniformly set to 40 h. The evolution of grout mechanical properties over time is described by Equation 15, and the corresponding variation curves of grout properties are illustrated in Figure 5.

$$\begin{cases} E(t) = E_g \cdot \left[1 - \exp\left(-\frac{0.3 \cdot t}{t_0}\right) \right] \\ \nu(t) = 0.3 + 0.2 \cdot \exp\left(-\frac{t}{5 \cdot t_0}\right) \end{cases} \quad (15)$$

In the equation, $E(t)$ represents the elastic modulus of the grout at time t , E_g is the elastic modulus of the grout after final setting, $\nu(t)$ denotes the Poisson’s ratio of the grout at time t , t_0 is the initial setting time of the grout, and t is the elapsed time since grout injection.

2.2.4 Simulation of grouting pressure and its dissipation

Due to the continuous operation of the grouting system, the maximum grouting pressure typically appears behind the first ring of segments at the shield tail. As the shield advances, the grouting

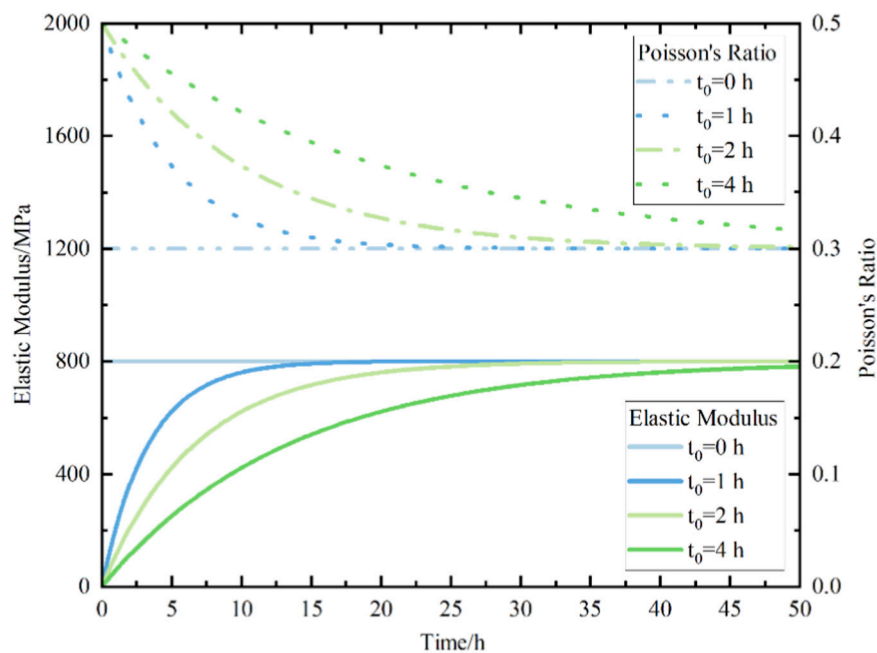


FIGURE 5
Variation of elastic modulus and Poisson's ratio of the grout with time.

pressure in this region dissipates accordingly. It is assumed that complete dissipation occurs over a distance equivalent to five segment rings. Given a typical advancement rate of six rings per day, and considering that the grouting pressure at the shield tail is initially equal to the ambient earth pressure and then decreases linearly, the grouting pressure can be expressed by Equation 16. Similarly, by combining the model spatial coordinates with the construction stage parameter, the grouting pressure can be defined such that both the vertical linear distribution and the axial linear dissipation of the pressure are accurately represented.

$$p = P \cdot k(t) = (150 + 10 \cdot h) \cdot (1 - t/20) \quad (16)$$

In Equation 16, h denotes the vertical depth of the grouting point measured from the ground surface. In the equation, p represents the grouting pressure, P represents the *in situ* environmental pressure, which also corresponds to the magnitude of the tunnel face support force, and $k(t)$ is the ratio of the current grouting pressure to the initial value at the time of injection. The constants 150 and 10 describe the initial shallow-ground pressure and its linear increase with depth, respectively, while the value 20 corresponds to the empirical dissipation duration of grouting pressure during shield tunneling.

2.3 Modeling and calculation

In constructing the model, the geological conditions at the site of Chongqing Metro Line 27 were considered. The detailed geological profile is shown in Figure 6. The ground strata were defined as mudstone, overlain by a 5-m layer of plain fill. The established model consists of a total of 393135 finite elements.

Material properties used in the simulation are listed in Table 1. Based on a typical section of Chongqing Metro Line 27, a finite element model of shield tunneling was developed using COMSOL Multiphysics, as illustrated in Figure 7. In the model, the positive direction of the y -axis corresponds to the tunnel excavation direction.

Based on the assumptions and analysis described above and considering that the grout hardening process spans ten segment rings as well as the need to minimize boundary effects, the model length along the tunnel axis was set to the equivalent of 50 segment rings. As a result, the numerical simulation domain was defined with dimensions of 45 m \times 90 m \times 45 m ($x \times y \times z$), respectively. The tunnel excavation diameter is $D = 8.83$ m, making the model length along the tunnel axis approximately 10.23D, and the width and height about 5.11D. These dimensions satisfy the commonly accepted range of 3–5 times the excavation diameter for minimizing boundary influence in tunnel simulations, allowing boundary effects to be reasonably neglected. To facilitate gravity loading, the vertical coordinate of the ground surface (Z) was set to 0 m. Similarly, the tunnel axis was aligned such that the X -coordinate at the centerline is 0 m, and the excavation starting point was assigned a Y -coordinate of 0 m.

The shield advancement rate was assumed to be six rings per day under ideal conditions. At each construction step, all associated processes—such as excavation, segment installation, grouting, and grout hardening—advance by exactly one ring. Therefore, an increment of one in the step parameter T corresponds to 4 h of actual construction time. Considering the time requirements of various construction processes, a total of 68 steps were required to complete the full construction sequence in the numerical model, which covers

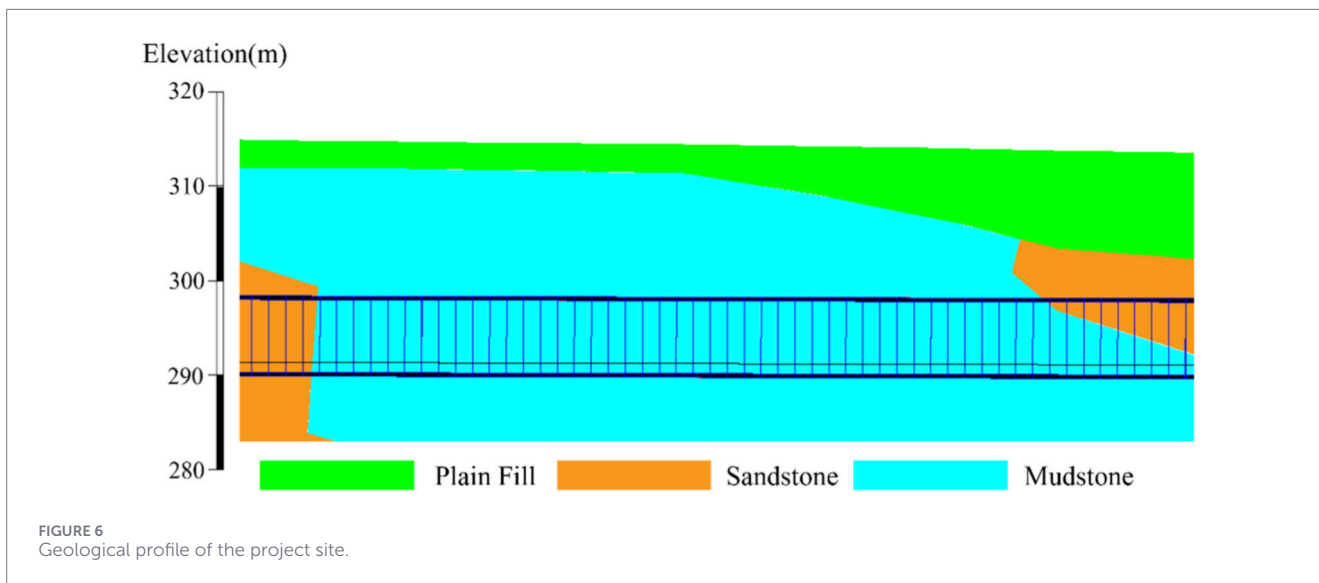


TABLE 1 Summary of material parameters used in the numerical model.

Material	Thickness/m	Density/kg·m ⁻³	Cohesion/kPa	Internal friction Angle/°	Elastic Modulus/MPa	Poisson's ratio
Plain fill	5	2000	0	28	15	0.3
Mudstone	16~35.2	2,550	468	32.6	1,342	0.32
Segment lining	0.4	2,500			24000	0.2
Shield machine	0.3	6,000			200000	0.15
Hardened grouting layer	0.165	2,200			800	0.3

a tunnel length of 50 segment rings along the tunnel axis. The key construction stages and their corresponding step parameters are summarized in Table 2.

3 Results

3.1 Vertical surface displacement

The development of vertical surface displacement at the middle cross-section perpendicular to the tunnel axis ($Y = 45\text{ m}$) is shown in Figure 8. It can be observed that the surface settlement in all models approximately follows a normal distribution, which is consistent with the surface loss theory proposed by Peck. Figure 8a illustrates the vertical surface displacement when the hardening process of the grout is not considered. When the cutterhead reaches the location, the vertical surface displacement is -0.26 mm , and it reaches -2.02 mm as the shield tail passes. Ultimately, the surface experiences a maximum settlement (most negative displacement) of -4.36 mm . The distribution of surface displacement for grout initial setting times of 1 h, 2 h, and 4 h is shown in Figures 8b–d. The maximum settlement (most negative displacement) reaches -5.60 mm , -6.51 mm , and -7.49 mm , which represent increases of

19%, 39%, and 59%, respectively, compared to the case with an initial setting time of 0 h.

3.2 Vertical displacement of strata

As shown in Figure 9, the final vertical displacements along the cross-sections at positions $x = 0\text{ m}$, 5 m , 10 m , 15 m , and 20 m on the middle cross-section ($Y = 45\text{ m}$) of the model are plotted. This is done to analyze the impact of different grout initial setting times on the vertical displacement of the surrounding strata. It can be observed that the further the distance from the tunnel center, the more stable the strata become.

When the initial setting time is 1 h, as shown in Figure 9a for the position $x = 0\text{ m}$: The strata above the tunnel exhibit settlement, and the settlement value fluctuates and increases with depth. Below the tunnel, a gradually decreasing heave is observed, with the maximum settlement and heave values at the crown and invert of the lining being -9.62 mm and 25.13 mm , respectively.

At position $x = 5\text{ m}$, as shown in Figure 9b, with increasing depth, the vertical displacement of the strata initially experiences settlement followed by heave. In the shallow layer ($z > -12\text{ m}$), the settlement value remains relatively stable at approximately

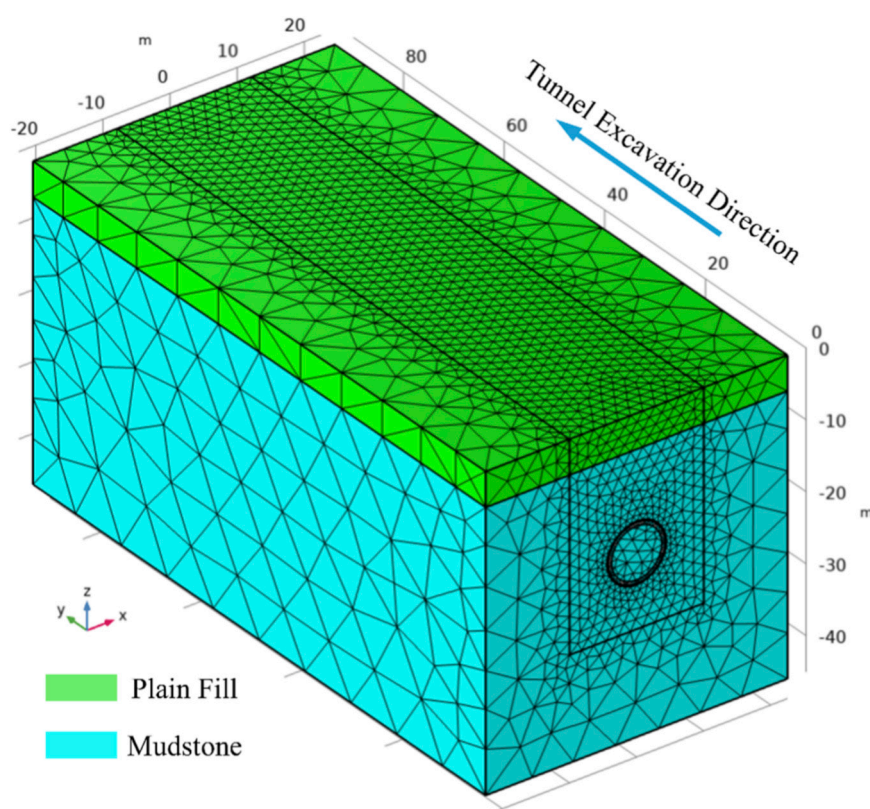


FIGURE 7 Finite element model of shield tunnel construction.

TABLE 2 Step parameters correspond to key simulation states in the model.

Step parameter T	Construction activity
0	Initial state
1	Cutterhead contact with model boundary
2~7	Shield machine entry
8~51	Shield tunneling, segment assembly, and synchronous grouting
52~57	Shield machine exit with completed segment and grouting works
58~62	Grout hardening and grouting pressure dissipation completed
63~67	Final grout hardening achieved

-4.9 mm. Subsequently, the settlement decreases rapidly and transforms into heave, reaching a maximum heave value of 9.29 mm near $z = -25$ m.

At position $x = 10$ m, as shown in Figure 9c, the vertical displacement of the strata with increasing depth shows the largest settlement at the surface, with a maximum value of -2.96 mm. At $z = -21$ m, the displacement reaches zero and then turns into heave, with the maximum heave value of 3.75 mm near $z = -31$ m.

At position $x = 15$ m, as shown in Figure 9d, the vertical displacement of the strata initially shows a maximum settlement value of -1.27 mm at the surface, which decreases until it reaches an inflection point at $z = -15$ m. The settlement then increases again, reaching -0.79 mm at $z = -22$ m. As the depth increases, the settlement value gradually decreases, and at $z < -30$ m, the vertical displacement of the strata turns into heave, with the maximum heave of 1.1 mm at $z = -36.5$ m.

At position $x = 20$ m, as shown in Figure 9e, with a grout initial setting time of 1 h, the vertical displacement of the strata first shows heave followed by settlement with increasing depth. The maximum heave of 0.22 mm is observed at $z = -9$ m, after which it decreases. At $z = -15$ m, the heave becomes zero, and at $z = -27$ m, the settlement reaches its inflection point with a maximum settlement value of -0.88 mm.

3.3 Horizontal displacement of strata

The development of horizontal strata displacement at a depth of $Z = -19.4$ m, which corresponds to the tunnel axis depth, is shown in Figure 10. The horizontal displacement follows an antisymmetric distribution about the tunnel axis.

Figure 10a illustrates the horizontal displacement development when the grout initial setting time is 0 h. Before the shield tail passes, the horizontal displacement is within 2 mm. As the shield tail passes and the grouting is performed, the horizontal

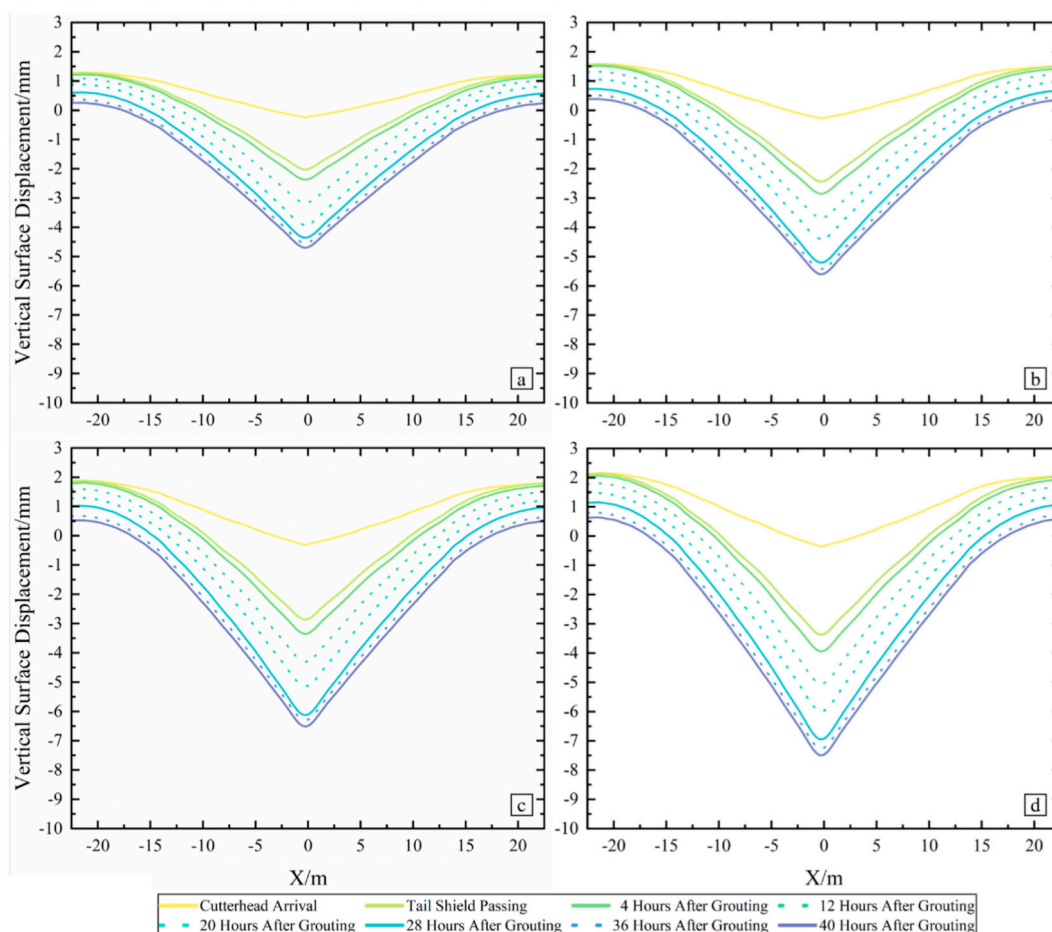


FIGURE 8
Development pattern of vertical surface displacement with different initial setting time: (a) 0 h, (b) 1 h, (c) 2 h, (d) 4 h.

displacement increases towards the tunnel arch waist along both sides of the model, reaching a maximum value of 5.5 mm. Subsequently, the horizontal displacement rebounds and decreases. After 4 h of grouting, the horizontal displacement at the tunnel arch waist decreases to 2.4 mm, and when the grouting pressure dissipates (20 h after grouting), it stabilizes at 2.1 mm. After 40 h of grouting, the horizontal displacement at the tunnel arch waist is 2.3 mm, which is a 58% reduction compared to the horizontal displacement at the time when the shield tail passed and grouting began.

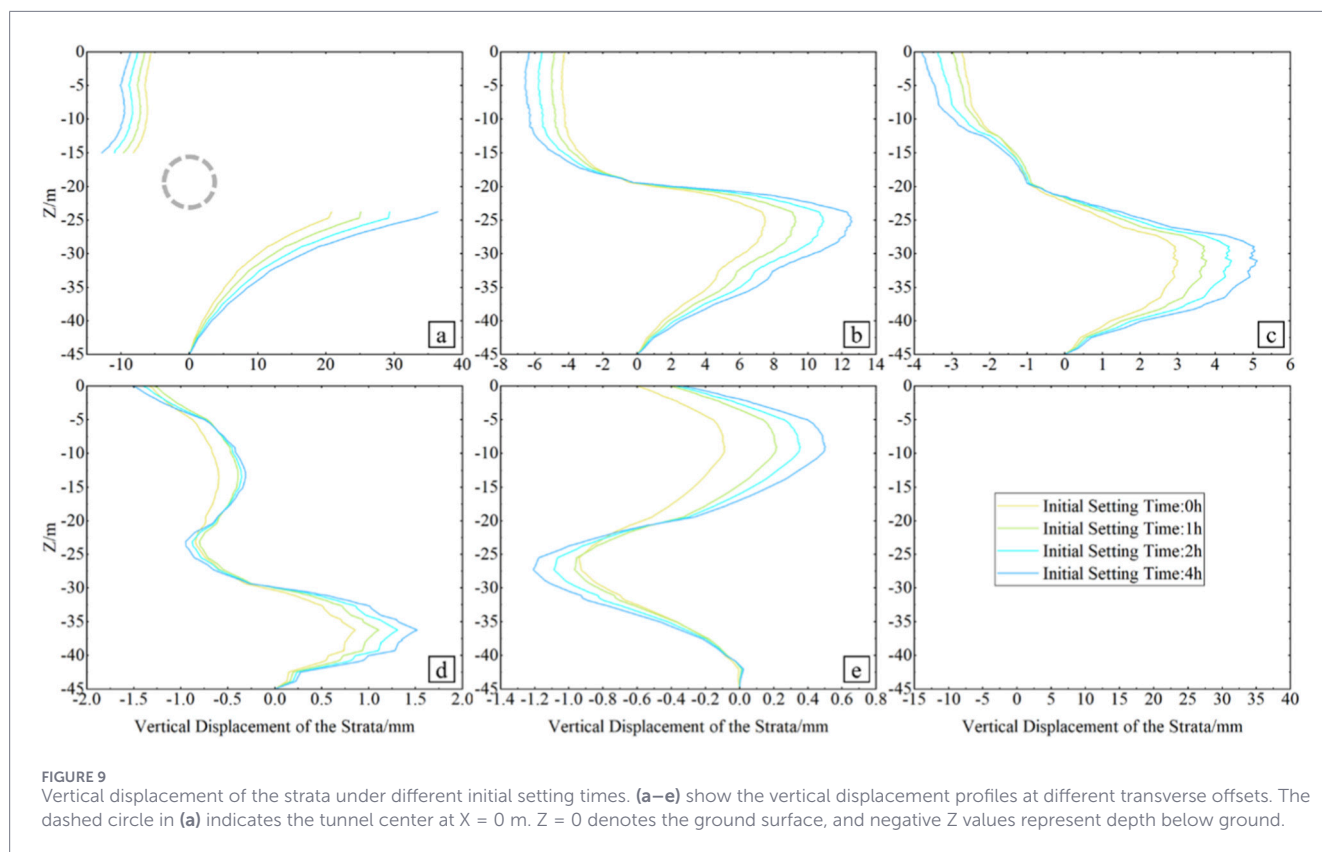
The development of horizontal displacement for grout initial setting times of 1 h, 2 h, and 4 h is shown in Figures 10b–d. During the grout hardening process, especially at the beginning of grouting, the slower the initial setting of the grout, the larger the horizontal displacement at the same moment. After 4 h of grouting, the horizontal displacements at the tunnel arch waist corresponding to the grout initial setting times of 1 h, 2 h, and 4 h are 2.4 mm, 3.1 mm, and 3.7 mm, respectively.

4 Discussion

4.1 Rationality of numerical simulation

The initial setting time used in the field is approximately 1 h. Therefore, the calculation results for a grout initial setting time of 1 h are compared with the data obtained from on-site monitoring. The vertical surface displacement variation at the center of the surface in the model is extracted and compared with the measured vertical surface displacement at the monitoring point above the tunnel axis in the project, as shown in Figure 11.

Clearly, the calculation results are in close agreement with the on-site monitoring data. This indicates that the established numerical model can reasonably reflect the actual strata response observed in the field. Furthermore, the model can converge the errors within a relative tolerance through iterative calculations, supporting the validity of the model.



4.2 Influence of initial setting time on surface displacement

Based on the variation patterns of vertical surface and strata displacement presented earlier, it can be concluded that vertical displacement magnitude increases as the grout initial setting time increases. Additionally, grouts with slower setting times, due to their delayed effect, reduce the supporting capacity of the strata, weakening the stress coordination ability of the strata. This leads to an increase in the vertical displacement difference between the strata on both sides of the tunnel. The large settlement zone caused by tunnel construction stabilizes within a range of 15 m on either side of the tunnel axis, with more significant increases in settlement values.

Furthermore, for the strata farther from the tunnel axis, the influence of a slower-setting grout layer results in more pronounced surface heave. This suggests a more apparent trend of overall shear deformation of the geotechnical body.

As the grout initial setting time increases, the maximum value of vertical settlement also increases. As seen in [Figure 9c](#), the depth at which the displacement value is zero gradually rises. This indicates that the increased grout initial setting time causes the strata at this depth to transition from settlement to heave. [Figure 9e](#) also shows that at certain depths; vertical displacement shifts from settlement to heave due to the delayed hardening process.

At the tunnel axis depth, horizontal displacement shows that the grout initial setting time has a minimal impact on the final horizontal displacement, with differences of less than

1 mm. This is likely due to the supporting effect of the grouting pressure. However, rapidly setting grout significantly reduces the maximum horizontal displacement of the strata immediately after the shield tail passes and grouting occurs, while also accelerating the rebound of horizontal displacement during the grouting process.

[Figure 12](#) shows the final surface vertical displacement for different grout initial setting times. Clearly, as the grout initial setting time increases, the surface vertical displacement significantly increases, and the rate of surface vertical displacement development also accelerates.

[Figure 13](#) shows the distribution of surface vertical displacement along the tunnel axis when the shield cutterhead reaches $Y = 72$ m (at this point, the grouting layer behind the 24th ring of lining is fully hardened, and the shield tail is at $Y = 61.2$ m). Clearly, for the four models with different grout initial setting times, the surface settlement reaches its maximum approximately two ring positions ($Y = 46.5$ m) before the grouting layer is fully hardened. The slower the grout hardens, the worse its control effect on surface settlement. When the grout initial setting times are 0 h, 1 h, 2 h, and 4 h, the maximum surface displacement above the tunnel axis is -4.13 mm, -4.97 mm, -5.83 mm, and -6.77 mm, respectively.

Moreover, the development of surface vertical displacement follows the same pattern in all four models. Before the cutterhead arrives, the surface exhibits slight heave due to the pressure from the cutterhead. As the cutterhead arrives, the surface vertical displacement rapidly develops into settlement. The rate of settlement growth reaches its maximum at the shield tail, with the surface

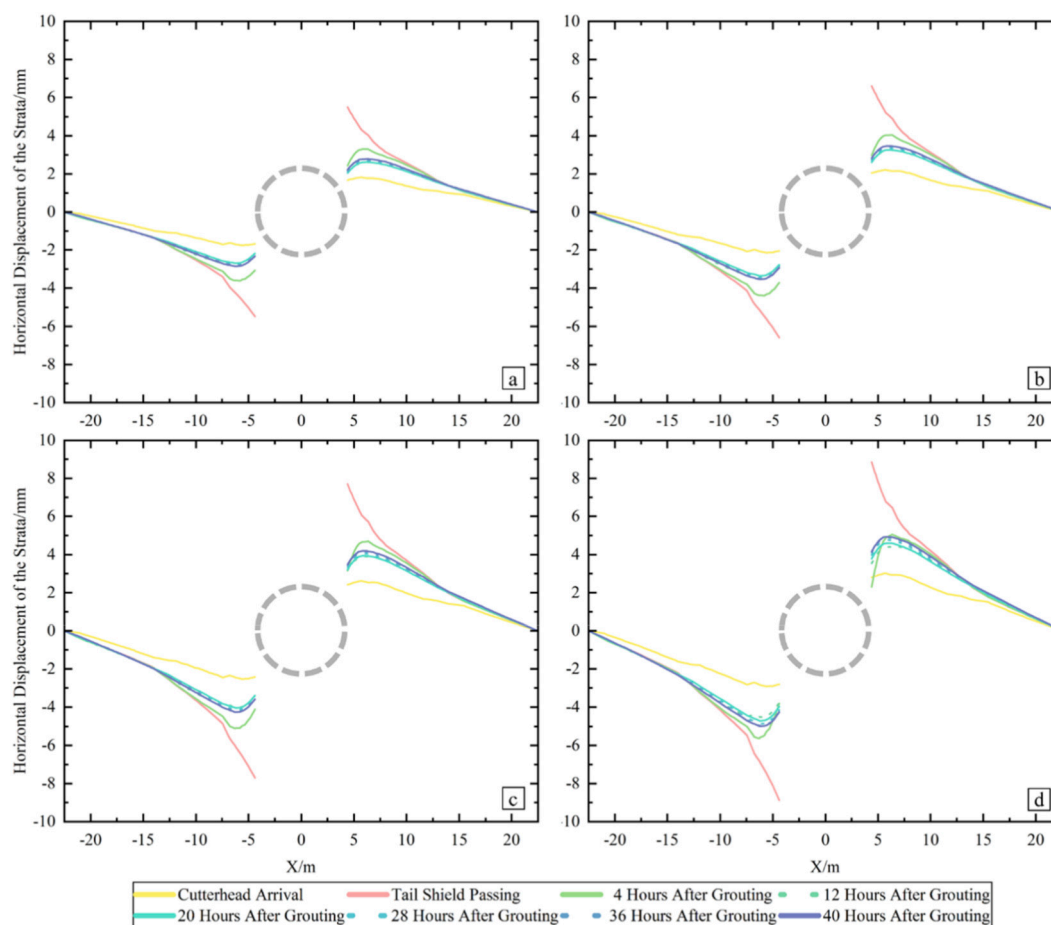


FIGURE 10 Development pattern of horizontal displacement in strata with different grout initial setting time: (a) 0 h, (b) 1 h, (c) 2 h, (d) 4 h. The circle denotes tunnel location; displacement discontinuity at $|X| = 4.4$ m occurs due to tunnel excavation.

settlement at this point being 0.5 times the maximum settlement value. After reaching the maximum settlement value, the surface settlement begins to rebound.

4.3 Comparison between theoretical calculation results and simulation results

The geotechnical tests conducted at the metro construction site indicate that the mudstone strata encountered by the tunnel exhibit a high Poisson’s ratio and a low elastic modulus. The low compressibility of the mudstone strata suggests that the error introduced by neglecting the surface vertical displacement caused by strata compression is acceptable. Additionally, as mudstone is a relatively weak rock formation, it is reasonable to approximate it as soil for calculation purposes.

For the Chongqing Metro Line 27, the shield excavation radius is 4.43 m. In this study, the tunnel axis depth is uniformly taken as $15 + 4.43$ m. Therefore, the calculated correction factor is 2.43. After analyzing the radial shrinkage data of the segments on-site, it was found that the shrinkage values of the segments are concentrated between 3.5 and 4.5 mm. Four frequently occurring values were selected for the calculation, namely: 3.6, 3.9, 4.1, and

4.4 mm. Additionally, to investigate which location, between the cutterhead and the shield tail, is more suitable as the point of $y = 0$ for the calculation, two calculation methods—where $y' = y$ and $y' = y + l$ —were employed to compute the surface vertical displacement.

Based on this, Figure 14 presents the surface vertical displacement along the y -direction calculated using the two methods, along with the surface deformation results obtained from numerical simulations at the same excavation position. Due to the size limitations of the numerical model, the simulation results do not cover the entire Y range. However, it can be observed that the surface vertical displacement range shown by the numerical simulation is smaller. Compared to the theoretical calculation results, surface vertical displacement in the numerical simulation begins to occur only when the cutterhead is closer, and it stabilizes earlier. This also indicates that the missing numerical simulation data has a negligible impact on the analysis in this study.

Moreover, it is evident from the numerical simulation results in the figure that surface vertical displacement significantly occurs at the shield tail. When using the method $y' = y + l$, when calculating with the original model, it is more reasonable to add the shield shell length to the value of y . Furthermore, it is observed that

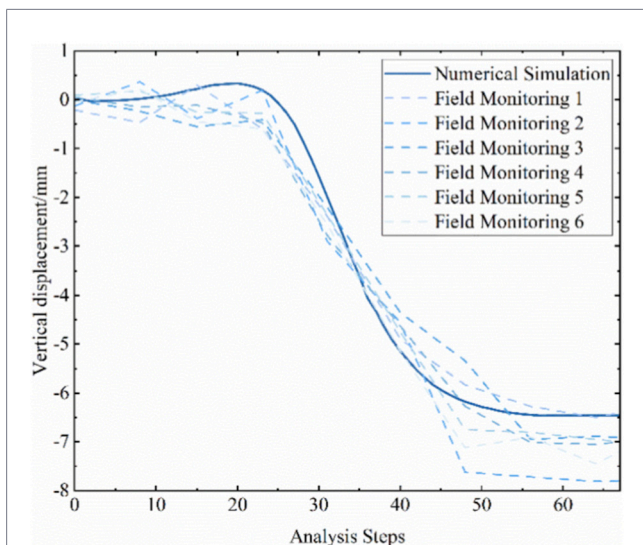


FIGURE 11
Comparison between numerical simulation results and field monitoring data. The monitoring data were obtained from routine surface vertical displacement measurements carried out at the project site using leveling points arranged along the tunnel alignment. The monitoring scheme consisted of multiple observation points spaced at regular intervals above the tunnel axis, with settlement recorded throughout the shield advancement process.

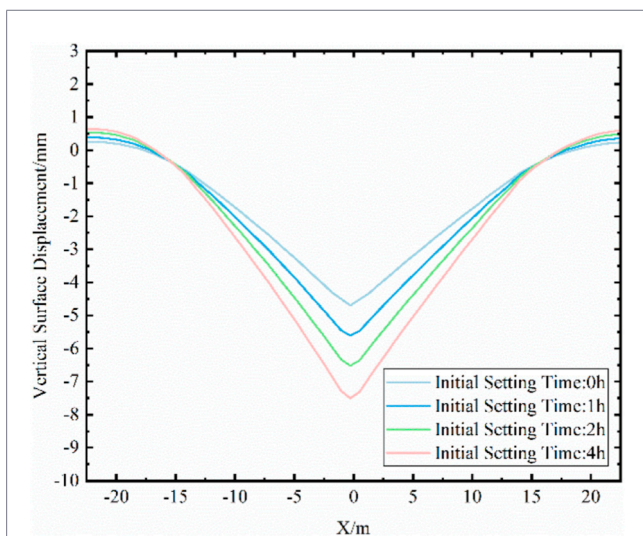


FIGURE 12
Final vertical surface displacement.

the numerical simulation results not only change more rapidly but also show a noticeably larger maximum settlement value. The on-site monitoring data shown in Figure 11 indicates that there is indeed slight heave on the surface before the cutterhead reaches the location. At the same time, the on-site monitoring results are slightly larger than the numerical simulation results, which suggests that the theoretical calculation of the maximum deformation is closer to the actual situation. However, the numerical simulation can predict the surface heave in front of the cutterhead, which highlights the advantage of the simulation.

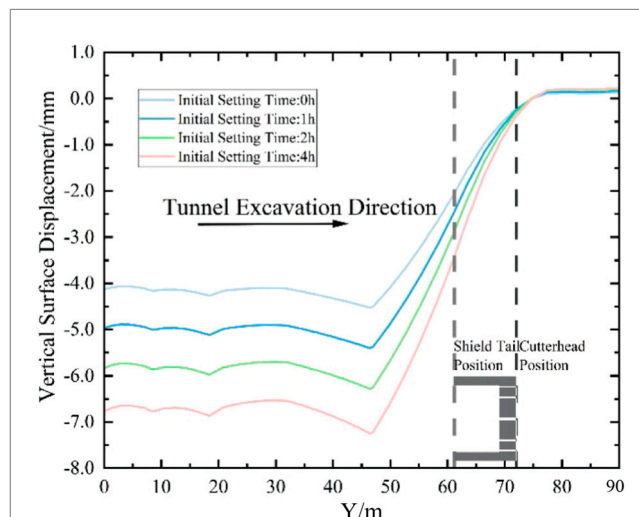


FIGURE 13
Surface vertical displacement distribution along the tunnel axis.

Figure 15 shows the surface vertical displacement along the x-direction at different locations using two calculation methods, compared with the numerical simulation results. (a), (b), (c), and (d) show the surface vertical displacement in four different states: when the cutterhead reaches the location, when the shield tail passes and grouting occurs, 20 h after grouting, and after the surface vertical displacement stabilizes. It is evident that the numerical simulation results change more rapidly over time. Clearly, the numerical simulation results exhibit a faster rate of change. Additionally, surface vertical displacement calculated using methods $y' = y$ and $y' = y + l$ gradually converge over time. However, before the deformation stabilizes, the results obtained using $y' = y + l$ generally fall between those of the other two methods.

4.4 Limitations of the deformation modeling framework and future work

Although this work combines analytical solutions with numerical modeling to quantify how grout setting and hardening affect construction-stage surface settlement in shallow-buried shield tunneling in mudstone strata, and identifies the shield tail as the critical longitudinal reference location for deformation development, several simplifications were adopted to keep the framework computationally efficient and suitable for systematic parametric evaluation. The main boundaries of applicability are summarized as follows.

1. Time-scale representation and long-term effects. The modeling focuses on construction-stage responses associated with synchronous grouting and early-age grout behavior, and it adopts a construction-step, quasi-static representation to efficiently evaluate the influence of grout setting time (0 h–4 h) (Wang et al., 2025). This approach captures the stabilized response relevant to the short time window of interest, but it does not reproduce detailed short-term transients immediately after grout injection and pressure dissipation,

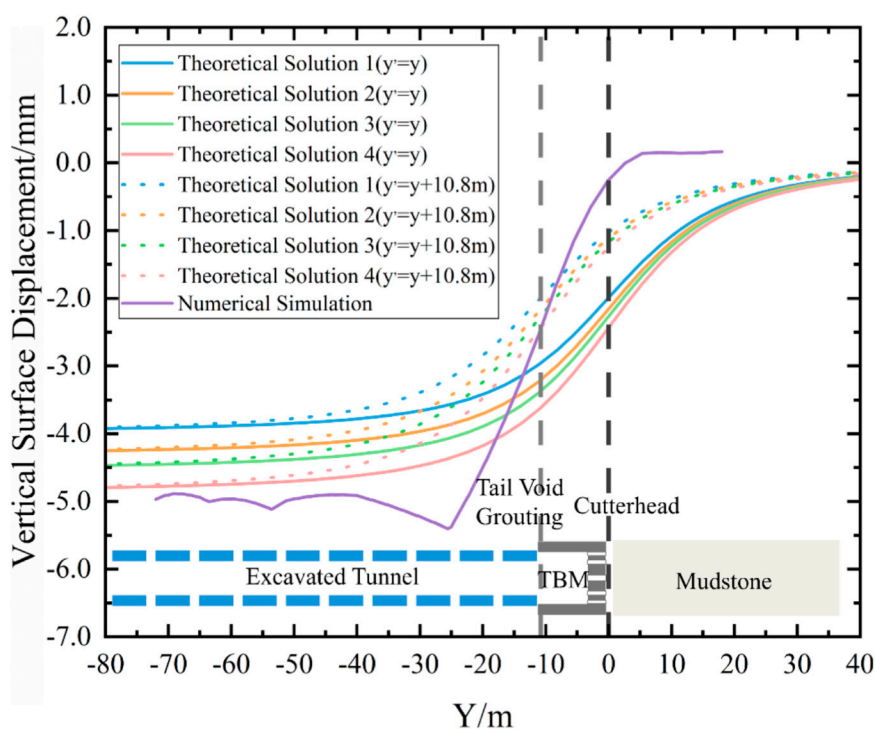


FIGURE 14
Theoretical calculation of surface vertical displacement above the tunnel axis.

nor does it address long-term rheological effects of mudstone (e.g., creep) that may become relevant over months to years (Wang et al., 2020; Yan et al., 2025). Fully time-dependent analyses and rheology-aware constitutive descriptions would be valuable when transient evolution or longer time scales are the focus.

- Material and structural idealizations. To isolate the role of grout setting and hardening, the grouting layer is represented with idealized, spatially uniform properties, and the surrounding ground is modeled without explicitly accounting for irregular defects, localized weak zones, or anisotropy associated with bedding and discontinuities in mudstone strata (Zhou et al., 2024; DeReuil et al., 2019; Bao et al., 2025). In the theoretical comparison, mudstone is idealized as a soil-like medium, which may not fully capture structural rock behavior and discontinuity effects (Liu B. et al., 2021). These simplifications help clarify dominant mechanisms and trends, but they may limit accuracy where strong spatial heterogeneity or structural control governs the response (Zhang et al., 2024a; b; Zhang et al., 2022). Future work could incorporate heterogeneous grouting representations and ground descriptions that account for anisotropy and discontinuities to better reflect site-specific complexity.
- Generalizability and parameter uncertainty. Model calibration and validation rely on a single engineering case (Chongqing Metro Line 27) and on available on-site monitoring and project parameters. Uncertainties in grouting pressure history, tail gap

evolution, local stratigraphic variability, and monitoring noise may influence the fitted correction parameters and the inferred sensitivity to grout setting time (Liu et al., 2025). Broader verification using multiple projects, together with uncertainty-aware parameter ranges (or simple uncertainty quantification), would strengthen generality and provide confidence bounds for predicted surface settlement.

5 Conclusion

This study investigates the surface deformation caused by the excavation of a shallow-buried shield tunnel in mudstone strata, using both theoretical models and numerical simulations, with a particular focus on the impact of grouting with different initial setting times on surface deformation. The results show that both numerical simulation and theoretical calculations can reliably capture the overall characteristics of surface deformation induced by shield tunneling. Numerical simulation remains advantageous for capturing localized responses such as the surface heave ahead of the cutterhead. The advantage of theoretical calculations is that they provide a more accurate estimate of the maximum surface settlement.

In the numerical simulation process, the results using a grout initial setting time of 1 h can effectively predict the surface deformation caused by shield tunnel excavation. This indicates that the assumptions and fittings of the grouting layer's mechanical properties are reasonable. Additionally, when using the theoretical

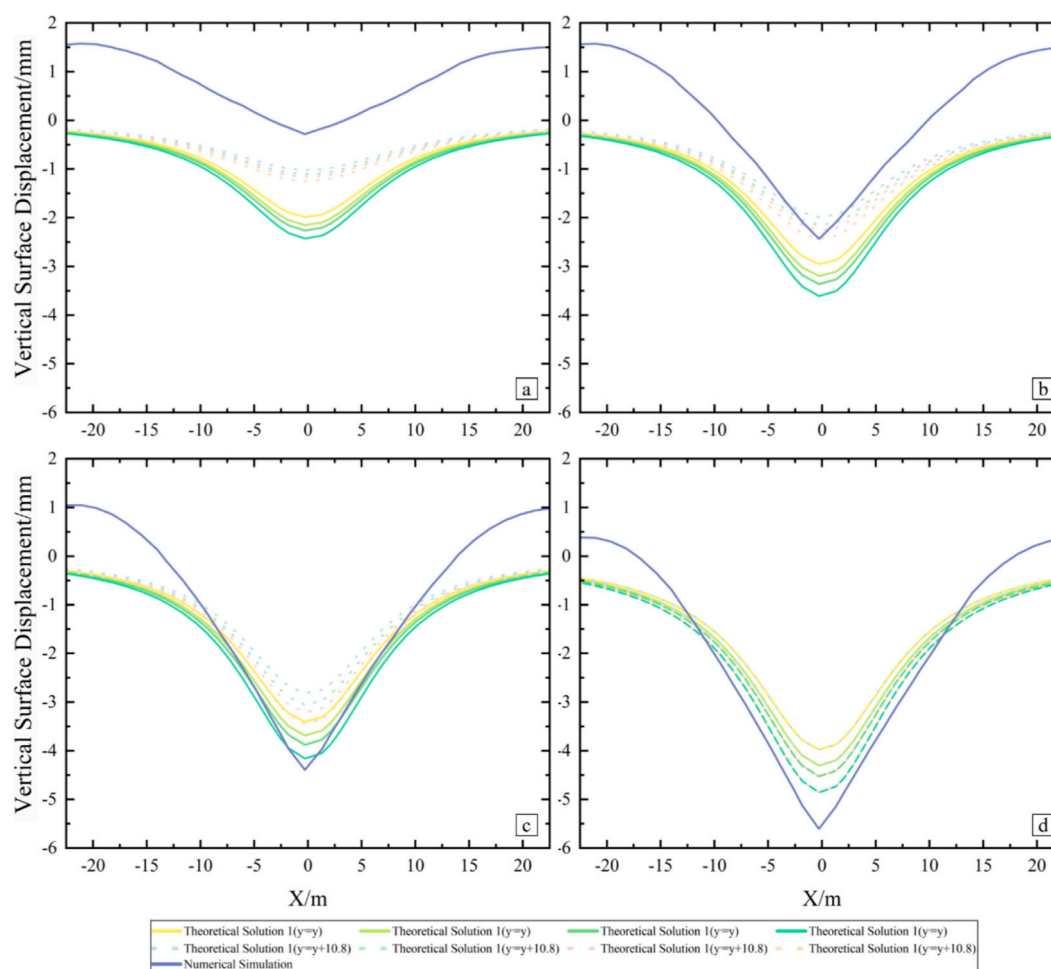


FIGURE 15

Theoretical calculation of surface vertical displacement in the x direction. (a) Cutterhead position, (b) shield tail position, (c) 20 h after grouting, (d) final state.

model for calculations, adding the shield shell length to the y-coordinate for the calculation aligns more closely with the rapid increase in deformation after the shield tail passes, which is confirmed by on-site monitoring results.

The calculated results show that, although deformation may rebound after a period, both vertical displacements of the surface and the strata increase with the hardening of the grout. Horizontal displacement in the strata behaves differently. This suggests that, when a shield tunnel crosses through mudstone strata, the presence of synchronous grouting increases the likelihood of vertical deformation in the strata, which leads to surface building damage. This is more probable than horizontal deformation, which may damage adjacent underground structures.

Specifically, accelerating the grout setting time is beneficial for controlling surface deformation during construction. Based on the comparative results of initial setting times from 0 h to 4 h, a practical initial setting time of approximately 1–2 h is recommended for engineering applications, as it provides effective deformation control without imposing excessive constraints on grouting operations. The longer the grout initial setting time, the slower the increase in the grout's mechanical properties and the later its support effect, which

leads to significantly higher surface loss and an increased likelihood of shear deformation in the strata. Reducing the initial setting time of the grout material can effectively control both vertical and horizontal displacements in the surface and strata.

Data availability statement

The original contributions presented in the study are included in the article/supplementary material, further inquiries can be directed to the corresponding author.

Author contributions

RZ: Conceptualization, Supervision, Validation, Writing – original draft, Writing – review and editing. XL: Data curation, Methodology, Validation, Writing – review and editing. YW: Conceptualization, Supervision, Writing – review and editing. ZQ: Resources, Validation, Writing – review and editing. ZH: Resources, Validation, Writing – review and editing. ML: Validation, Writing –

review and editing. ZJ: Conceptualization, Funding acquisition, Supervision, Writing – review and editing.

Funding

The author(s) declared that financial support was not received for this work and/or its publication.

Conflict of interest

Author RZ was employed by Chongqing Rail Transit Design and Research Institute Company. Authors XL, YW, ZQ, ZH, and ML were employed by Powerchina Sinohydro Engineering Bureau 4 Co., Ltd.

The remaining author(s) declared that this work was conducted in the absence of any commercial or financial relationships that could be construed as a potential conflict of interest.

References

- Abdelaziz, A., Islam, M. S., and Iskander, M. (2023). Longitudinal settlements during tunneling in soft clay, using transparent soil models. *Tunn. Undergr. Space Technol.* 136, 105042. doi:10.1016/j.tust.2023.105042
- Ağbay, E., and Topal, T. (2020). Evaluation of twin tunnel-induced surface ground deformation by empirical and numerical analyses (natm part of eurasia tunnel, Turkey). *Comput. Geotechnics* 119, 103367. doi:10.1016/j.compgeo.2019.103367
- Alsahly, A., Stascheit, J., and Meschke, G. (2016). Advanced finite element modeling of excavation and advancement processes in mechanized tunneling. *Adv. Eng. Softw.* 100, 198–214. doi:10.1016/j.advengsoft.2016.07.011
- Alsirawan, R., Sheble, A., and Alnmr, A. (2023). Two-dimensional numerical analysis for tbm tunneling-induced structure settlement: a proposed modeling method and parametric study. *Infrastructures* 8, 88. doi:10.3390/infrastructures8050088
- Anato, N. J., Chen, J., Tang, A., and Assogba, O. C. (2021). Numerical investigation of ground settlements induced by the construction of nanjing weisanlu tunnel and parametric analysis. *Arabian J. Sci. Eng.* 46, 11223–11239. doi:10.1007/s13369-021-05642-3
- Bao, S., Wang, H., Yang, Y., He, Y., Li, Z., and Zhai, C. (2025). Study on mechanical properties of sand-mudstone interbedded rock mass under different layer thickness ratio-dip angle conditions. *KSCSE J. Civ. Eng.* 29 (11), 100252. doi:10.1016/j.kscsej.2025.100252
- Cao, S., Liang, R., Kang, C., Wu, W., Ke, Z., and Guo, Y. (2024). Analytical prediction for longitudinal deformation of shield tunnel subjected to ground surface surcharge considering the stiffness reduction. *Int. J. Numer. Anal. Methods Geomechanics* 48, 925–950. doi:10.1002/nag.3673
- Cui, Z. D., Zhu, Z. L., Mi, X. Y., Yuan, L., Zhang, Z. L., and Zhao, C. Y. (2024). Effect of shield tunnel underpass construction on the upper existing pipeline. *Geomechanics Eng.* 39, 369–383. doi:10.12989/gae.2024.39.4.369
- Deng, H., Fu, H., Shi, Y., Huang, Z., and Huang, Q. (2021). Analysis of asymmetrical deformation of surface and oblique pipeline caused by shield tunneling along curved section. *Symmetry* 13, 2396. doi:10.3390/sym13122396
- DeReuil, A. A., Birgenheier, L. P., and McLennan, J. (2019). Effects of anisotropy and saturation on geomechanical behavior of mudstone. *J. Geophys. Res. Solid Earth* 124 (8), 8101–8126. doi:10.1029/2018JB017034
- Ding, Z., He, S. Y., Zhou, W. H., Xu, T., He, S. H., and Zhang, X. (2021). Analysis of ground deformation induced by shield tunneling considering the effects of muck discharge and grouting. *Transp. Geotech.* 30, 100629. doi:10.1016/j.trgeo.2021.100629
- Dong, Y., Ding, Z., Jiang, Y., Chen, C., Shen, W., and Wang, Y. (2022). Measured analysis on surface deformation and influence of cutter torque for twin shield tunnelling in silty sand. *Adv. Civ. Eng.* 2022, 9839798. doi:10.1155/2022/9839798
- Fang, Y. S., Wu, C. T., Chen, S. F., and Liu, C. (2014). An estimation of subsurface settlement due to shield tunneling. *Tunn. Undergr. Space Technol.* 44, 121–129. doi:10.1016/j.tust.2014.07.015
- Franzius, J. N., Potts, D. M., Addenbrooke, T. I., and Burland, J. B. (2004). The influence of building weight on tunnelling-induced ground and building deformation. *Soils Found.* 44, 25–38. doi:10.3208/sandf.44.25

Generative AI statement

The author(s) declared that generative AI was not used in the creation of this manuscript.

Any alternative text (alt text) provided alongside figures in this article has been generated by Frontiers with the support of artificial intelligence and reasonable efforts have been made to ensure accuracy, including review by the authors wherever possible. If you identify any issues, please contact us.

Publisher's note

All claims expressed in this article are solely those of the authors and do not necessarily represent those of their affiliated organizations, or those of the publisher, the editors and the reviewers. Any product that may be evaluated in this article, or claim that may be made by its manufacturer, is not guaranteed or endorsed by the publisher.

Goh, A. T. C., Zhang, W., Zhang, Y., Xiao, Y., and Xiang, Y. (2018). Determination of Earth pressure balance tunnel-related maximum surface settlement: a multivariate adaptive regression splines approach. *Bull. Eng. Geol. Environ.* 77, 489–500. doi:10.1007/s10064-016-0937-8

Han, H., Zhang, W., Wu, Z., and Sun, W. (2025). Probabilistic analysis of tunnel deformation and ground surface settlement induced by surcharge in spatially variable soil. *Comput. Geotechnics* 186, 107369. doi:10.1016/j.compgeo.2025.107369

Huang, Z., Zhang, H., Fu, H., Ma, S., and Liu, Y. (2020). Deformation response induced by surcharge loading above shallow shield tunnels in soft soil. *KSCSE J. Civ. Eng.* 24, 2533–2545. doi:10.1007/s12205-020-0404-8

Kasper, T., and Meschke, G. (2006). A numerical study of the effect of soil and grout material properties and cover depth in shield tunnelling. *Comput. Geotechnics* 33, 234–247. doi:10.1016/j.compgeo.2006.04.004

Kavvasas, M., Litsas, D., Vazaios, I., and Fortsakis, P. (2017). Development of a 3d finite element model for shield epb tunnelling. *Tunn. Undergr. Space Technol.* 65, 22–34. doi:10.1016/j.tust.2017.02.001

Komiya, K., Soga, K., Akagi, H., Jafari, M. R., and Bolton, M. D. (2001). Soil consolidation associated with grouting during shield tunnelling in soft clayey ground. *Geotechnique* 51, 835–846. doi:10.1680/geot.51.10.835.41062

Kong, F., Lu, D., Du, X., and Shen, C. (2019). Displacement analytical prediction of shallow tunnel based on unified displacement function under slope boundary. *Int. J. Numer. Anal. Methods Geomechanics* 43, 183–211. doi:10.1002/nag.2859

Kong, F., Lu, D., Ma, Y., Li, J., and Tian, T. (2022). Analysis and intelligent prediction for displacement of stratum and tunnel lining by shield tunnel excavation in complex geological conditions: a case study. *Ieee Trans. Intelligent Transp. Syst.* 23, 22206–22216. doi:10.1109/ITITS.2022.3149819

Lambrughi, A., Medina Rodriguez, L., and Castellanza, R. (2012). Development and validation of a 3d numerical model for tbm-epb mechanised excavations. *Comput. Geotechnics* 40, 97–113. doi:10.1016/j.compgeo.2011.10.004

Liang, J., Liu, W., Yin, X., Li, W., Yang, Z., and Yang, J. (2025). Experimental study on the performance of shield tunnel tail grout in ground. *Undergr. Space (new)* 20, 277–292. doi:10.1016/j.undsp.2024.07.001

Liu, B., Yang, H., and Karekal, S. (2021). Reliability analysis of TBM disc cutters under different conditions. *Underground Space (China)* 6, 142–152. doi:10.1016/j.undsp.2020.01.001

Liu, C., Cui, J., Zhang, Z. X., Liu, H., Huang, X., and Zhang, C. Q. (2021). The role of tbm asymmetric tail-grouting on surface settlement in coarse-grained soils of urban area: field tests and fea modelling. *Tunn. Undergr. Space Technol.* 111, 103857. doi:10.1016/j.tust.2021.103857

Liu, W., Liang, J., and Xu, T. (2023). Tunnelling-induced ground deformation subjected to the behavior of tail grouting materials. *Tunn. Undergr. Space Technol.* 140, 105253. doi:10.1016/j.tust.2023.105253

Liu, F., Chen, W., Liu, C., Yang, Y., Wang, J., and Liu, Y. (2025). The evolution of grouting pressure and ground deformation induced by synchronous grouting during

- shield tunneling in soft soil: an investigation based on scaled model test and CEL simulation. *Can. Geotechnical J.* 62, 1–20. doi:10.1139/cgj-2024-0378
- Lou, P., Li, Y., Xiao, H., Zhang, Z., and Lu, S. (2022). Influence of small radius curve shield tunneling on settlement of ground surface and mechanical properties of surrounding rock and segment. *Appl. Sci. Switz.* 12, 9119. doi:10.3390/app12189119
- Mair, R. J., Taylor, R. N., and Bracegirdle, A. (1993). Subsurface settlement profiles above tunnels in clays. *Geotechnique* 43, 315–320. doi:10.1680/geot.1993.43.2.315
- Meng, F. Y., Chen, R. P., and Kang, X. (2018). Effects of tunneling-induced soil disturbance on the post-construction settlement in structured soft soils. *Tunn. Undergr. Space Technol.* 80, 53–63. doi:10.1016/j.tust.2018.06.007
- Mindlin, R. D., and Cheng, D. H. (1950). Thermoelastic stress in the semi-infinite solid. *J. Appl. Phys.* 21, 931–933. doi:10.1063/1.1699786
- Mooney, M. A., Grasmick, J., Kenneally, B., and Fang, Y. (2016). The role of slurry tbm parameters on ground deformation: field results and computational modelling. *Tunn. Undergr. Space Technol.* 57, 257–264. doi:10.1016/j.tust.2016.01.007
- Ocak, I. (2014). A new approach for estimating the transverse surface settlement curve for twin tunnels in shallow and soft soils. *Environ. Earth Sci.* 72, 2357–2367. doi:10.1007/s12665-014-3145-5
- Peck, R. B. (1969). “Deep excavation and tunnelling in soft ground. state-Of-The-art report,” in *Proceedings of 7th international conference on soil mechanics and foundation engineering* (Mexico City), 225–290.
- Pinto, F., and Whittle, A. J. (2014). Ground movements due to shallow tunnels in soft ground. I: analytical solutions. *J. Geotechnical Geoenvironmental Eng.* 140, 04013040. doi:10.1061/(asce)gt.1943-5606.0000948
- Qiao, J., Liu, J., Guo, W., and Zhang, Y. (2010). Artificial neural network to predict the surface maximum settlement by shield tunneling. *Intelligent Robotics And Applications.* 6424, 257–265. doi:10.1007/978-3-642-16584-9_24
- Sagaseta, C. (1987). Analysis of undrained soil deformation due to ground loss. *Geotechnique* 37, 301–320. doi:10.1680/geot.1987.37.3.301
- Sen, B. (1951). Note on the stresses produced by nuclei of thermo-elastic strain in a semi-infinite elastic solid. *Q. Appl. Math.* 8, 365–369. doi:10.1090/qam/37717
- Shahin, H. M., Nakai, T., Ishii, K., Iwata, T., and Kuroi, S. (2016). Investigation of influence of tunneling on existing building and tunnel: model tests and numerical simulations. *Acta Geotech.* 11, 679–692. doi:10.1007/s11440-015-0428-2
- Shi, C., Cao, C., and Lei, M. (2017). An analysis of the ground deformation caused by shield tunnel construction combining an elastic half-space model and stochastic medium theory. *KSCE J. Civ. Eng.* 21, 1933–1944. doi:10.1007/s12205-016-0804-y
- Song, K., Yang, H., and Wang, Z. (2023). A hybrid stacking framework optimized method for tbm performance prediction. *Bull. Eng. Geol. Environ.* 82, 27. doi:10.1007/s10064-022-03047-6
- Tian, Z., Yu, C., Zhang, B., Zhao, Q., and Wang, Z. (2023). Analysis of surface and building deformation by shield tunneling through geology. *Appl. Sci. Switz.* 13, 11155. doi:10.3390/app132011155
- Verruijt, A., and Booker, J. R. (1996). Surface settlements due to deformation of a tunnel in an elastic half plane. *Geotechnique* 46, 753–756. doi:10.1680/geot.1996.46.4.753
- Wang, Z. S., Wang, M. S., and Zhang, M. (2009). Methods for estimating subsurface ground movements induced by shield tunneling. *Yantu Lixue/Rock Soil Mech.* 30, 1699–1704.
- Wang, S., He, C., Nie, L., and Zhang, G. (2019). Study on the long-term performance of cement-sodium silicate grout and its impact on segment lining structure in synchronous backfill grouting of shield tunnels. *Tunn. Undergr. Space Technol.* 92, 103015. doi:10.1016/j.tust.2019.103015
- Wang, J. G., Sun, Q. L., Liang, B., Yang, P. J., and Yu, Q. R. (2020). Mudstone creep experiment and nonlinear damage model study under cyclic disturbance load. *Sci. Rep.* 10 (1), 9305. doi:10.1038/s41598-020-66245-w
- Wang, X., Li, S., Wei, Y., and Zhang, Y. (2022). Analysis of surface deformation and settlement characteristics caused by tunnel excavation and unloading. *Geofluids* 2022, 1–15. doi:10.1155/2022/5383257
- Wang, S., Zeng, H., Chen, X., Zheng, X., Zhang, C., and Ni, Z. (2025). Time-varying strength characteristics of synchronous grouting materials derived from geopolymer-modified shield muck. *J. Clean. Prod.* 536, 147121. doi:10.1016/j.jclepro.2025.147121
- Yan, H., Yu, F., Zhu, C., Yuan, J., Wang, Q., and Wu, J. (2025). A new swelling-creep model for red-bed mudstone and its application. *Front. Earth Sci.* 13, 1577262. doi:10.3389/feart.2025.1577262
- Yang, H., Liu, F., and Lin, S. (2020). Investigation on the 3d ground settlement induced by shallow tunneling considering the effects of buildings. *KSCE J. Civ. Eng.* 24, 365–376. doi:10.1007/s12205-020-2201-9
- Yang, J., Yin, Z. Y., Liu, Y. J., and Laouafa, F. (2023). Multiphysics modelling of backfill grouting in sandy soils during tbm tunnelling. *Acta Geotech.* 18, 553–571. doi:10.1007/s11440-022-01528-2
- Zhang, J. B., Zhang, X. H., Chen, W., Huang, Z., and Du, R. H. (2022). A constitutive model of freeze-thaw damage to transversely isotropic rock masses and its preliminary application. *Comput. Geotechnics* 152, 105056. doi:10.1016/j.compgeo.2022.105056
- Zhang, Q., Zhang, X. P., Wang, H. J., Zhang, X. Y., Li, F. Y., and Xu, D. (2023). Ground deformation induced by a shallow-buried twin-tunnel with small spacing: a case study of guangzhou metro line 18 excavated by earth-pressure balance tbm. *Environ. Earth Sci.* 82, 297. doi:10.1007/s12665-023-10993-1
- Zhang, J. B., Du, R. H., Zhang, X. H., Huang, Z., and Zhang, W. J. (2024a). The deformation and failure characteristics of tunnels in layered rock with gentle dip angles after freeze-thaw cycles: physical model tests and numerical investigation. *Tunn. Undergr. Space Technol.* 144, 105527. doi:10.1016/j.tust.2023.105527
- Zhang, J. B., Chen, Y. L., Du, R. H., Zhao, X. L., and Wu, J. (2024b). Macroscopic and microscopic mechanical characteristics and crack propagation behavior of sandstone-like samples with single cracks under freeze-thaw cycles: experimental and numerical simulation. *Theor. Appl. Fract. Mech.* 129, 104201. doi:10.1016/j.tafmec.2023.104201
- Zheng, G., Pan, J., Cheng, X., Bai, R., Du, Y., Diao, Y., et al. (2020). Use of grouting to control horizontal tunnel deformation induced by adjacent excavation. *J. Geotechnical Geoenvironmental Eng.* 146, 05020004. doi:10.1061/(ASCE)GT.1943-5606.0002276
- Zhou, Z., Ding, H., Miao, L., and Gong, C. (2021). Predictive model for the surface settlement caused by the excavation of twin tunnels. *Tunn. Undergr. Space Technol.* 114, 104014. doi:10.1016/j.tust.2021.104014
- Zhou, H., Zhang, Y., Zhu, W., Zhong, Q., and Huang, X. (2024). Optimisation of synchronous grouting mix ratio for shield tunnels. *Appl. Sci.* 14 (10), 4098. doi:10.3390/app14104098